1

Background and Basic Knowledge of Perovskite Solar Cells

Maria Vasilopoulou[1], *Abd Rashid B. Mohd Yusoff*[2], *and*
Mohammad K. Nazeeruddin[3]

[1] *National Centre for Scientific Research Demokritos, Institute of Nanoscience and Nanotechnology, Agia Paraskevi, 15341 Attica, Greece*
[2] *Pohang University of Science and Technology(POSTECH), Department of Chemical Engineering, Pohang, Gyeongbuk, 37673, Republic of Korea*
[3] *École Polytechnique Fédérale de Lausanne (EPFL), Institute of Chemical Sciences and Engineering, Group for Molecular Engineering of Functional Materials, Rue de l'Industrie 17, CH-1951, Sion, Switzerland*

1.1 Background

The deployment of renewable energy sources lies within the context of prohibiting climate change and achieving greenhouse gas reduction targets [1]. Solar energy is clean and abundant; therefore, its usage can fulfill the need for sustainable development in order to protect the environment by limiting the consumption of fossil fuels. Photovoltaic systems convert the sun's energy directly into electricity through the application of semiconductor materials that utilize the so-called photovoltaic effect or photovoltaic phenomenon.

The photovoltaic phenomenon was first reported in 1839 by 19-year-old Edmund Becquerel, who was able to produce weak electrical current in a prototype cell by employing a silver-coated platinum electrode immersed in certain electrolytes, which was exposed to sunlight. He called this phenomenon the "photovoltaic effect," which is the basic principle that governs solar cell operation that converts sunlight into electricity [2]. However, it was about forty years later, in 1876, when the first solid-state photovoltaic cell was demonstrated by William Adams and Richard Day [3]. It employed a junction formed between selenium (Se) and platinum (Pt) which produced electricity without having moving parts and led to the development of modern solar cell systems. Adams and Day also found that "the ultra-red or the ultraviolet rays have little or no effect on the production of energy." They also observed that the produced electricity was highly dependent on the illuminating power of the light, "being directly related to the square root of that illuminating power" [4]. A few years later, in 1883, Charles Fritts fabricated the first large-area solar cell by pressing a selenium layer between two thin gold metal foils [5].

In the following years, photovoltaic effects were also observed in other semiconductor materials such as copper–copper oxide (Cu:CuO) thin-film heterostructures,

Printable Mesoscopic Perovskite Solar Cells, First Edition.
Edited by Hongwei Han, Michael Grätzel, Anyi Mei, and Yue Hu.

lead sulfide (PbS), and thallium sulfide (TlS). In these early devices, a thin semi-transparent metal layer was deposited on the semiconductor material to provide an asymmetric Schottky junction without prohibiting light from reaching the semiconductor. The discovery of silicon (Si) p–n junction in the 1950s offered a significant boost to the development of solar cells as these p–n junction structures exhibited better rectifying ability than the Schottky ones and hence delivered better photovoltaic behavior. The first Si solar cell was reported by Chapin, Fuller, and Pearson in 1954 and converted sunlight to electricity with an efficiency of 6% [6]. These pioneers used their solar panels to power a small toy Ferris wheel and a solar-powered radio transmitter. A few years later, in 1957, they increased the efficiency to 8% [7]. Notably, a solar cell based on cadmium sulfide (CdS) p–n junction was demonstrated in 1954, also producing electricity with an efficiency of 6%.

During the next decades, interest in photovoltaics expanded to other semiconductor materials such as gallium arsenide (GaAs), indium phosphide (InP), and cadmium telluride (CdTe), which, unlike Si, possess a direct bandgap, and theoretical work indicated that they could offer higher efficiency. Afterward, the growing awareness of the need to make use of an alternative to fossil fuel sources of electricity led photovoltaic production to be expanded at a rate of 15–25% per year. This has also driven a sufficient cost reduction which made photovoltaics competitive for increase in supply in grid-connected loads at peak use and in contexts where the conventional electricity supply was quite expensive, for example, in remote low-power applications such as telecommunications, navigation, and rural electrification. However, new markets have opened up such as building integrated photovoltaics, where besides the efficiency and cost of the photovoltaic system, its easy integration in building facades and roofs can be facilitated by using alternative solution-based materials and fabrication methods.

1.2 The Principle of Solar Cells

1.2.1 Silicon Solar Cells

A solar cell is an optoelectronic device based on a p–n junction formed between two oppositely doped regions of a single semiconductor material, a p–type which has an excess of free holes and n-type having an excess of free electrons [2]. The p-type and n-type regions in a Si p–n junction are created by using appropriate trivalent (acceptor, having three valence electrons like boron, B; aluminum, Al; gallium, Ga; and indium, In) and pentavalent (donor, like phosphorus, P; antimony, Sb; and arsenic, As) impurities (dopants), respectively, via ion implantation, epitaxy, or diffusion of dopants. Because the Si semiconductor owns four valence electrons, doping with acceptors creates an excess of holes, while doping with donors results in the formation of nearly free electrons. Consequently, the concentration of free holes is much higher in the p-type region compared to the n-type region and *vice versa* (free electrons are much more in the n-type region), which creates a high concentration gradient of charge carriers across the junction line.

Considering the energy diagram, the Fermi level (E_F) shifts toward the valence band (VB) maximum in the p-type region and toward the conduction band (CB) minimum in the n-type region, hence creating a discontinuity in energy across the p–n junction. As a result, free holes (majority carriers) diffuse from the p-type region toward the junction line, while electrons diffuse from the n-type region and cross the p–n junction where they subsequently recombine with holes leaving negatively charged acceptor and positively charged donor ions at the p-type and n-type regions, respectively. These charged ions continue to increase and, because they are immobile, they build an electric field which is directed from the n-type to p-type region of the junction.

Due to this internal electric field, minority carriers (which are holes from the n-type region and electrons from the p-type region) drift toward the opposite region and eventually balance and stop the diffusive flow of majority carriers. At this stage of equilibrium, the two charged ionic "layers" on either side of the p–n junction form the so-called space charge region of the diode. This central region is also called as "depletion region" because it is depleted of free carriers; holes have left the space $-x_{p0} \leq x < 0$ in the p-type region and electrons have left the space $0 \leq x \leq x_{n0}$ in the n-type region, where $x = 0$ corresponds to p–n junction line. As a result, for $x_{p0} \leq x \leq x_{n0}$, we have $np < n_i^2$, where n, p are the concentration of free electrons and holes in the doped semiconductor, and n_i (equal to p_i) is the concentration of electrons (holes) in the intrinsic material before doping. The width of the depletion region is $W = x_{n0} + x_{p0}$. Note that, deep in the p-type and in the n-type regions, the semiconductor remains quasi-neutral, having a concentration of free holes $p = N_A$ and of free electrons $n = N_D$ in these quasi-neutral p and n regions, where N_A and N_D are the concentrations of acceptor and donor dopants, respectively.

The internal electric field of the p–n junction defines a voltage barrier which is called the device's "built-in" potential, V_{bi}, that prohibits further movement of free carriers, and the diode enters an equilibrium phase where the drift current of the minority carriers becomes equal to the diffusion current of majority carriers, hence eliminating each other. This potential is defined by the following equation:

$$\begin{aligned} V_{bi} &= E_{Fn0} - E_{Fp0} = E_i + k_B T \ln\left(\frac{N_D}{n_i}\right) - E_i + k_B T \ln\left(\frac{N_A}{n_i}\right) \\ &= k_B T \ln\left(\frac{N_D N_A}{n_i^2}\right) \end{aligned} \tag{1.1}$$

If we consider the band diagram of the semiconductor just before the p–n region is formed, the conduction and VB edges will line up at both sides, while the Fermi level will exhibit a discontinuity at the junction (due to different positioning between E_{Fp} and E_{Fn} that correspond to the Fermi levels of p-type and n-type semiconductors and lie near the VB maximum and CB minimum, respectively, while E_{Fi} corresponds to the Fermi level of an intrinsic semiconductor and lies at the middle of the bandgap, Figure 1.1a). Statistical mechanics demands that at equilibrium where the diffusion of opposite carriers is prohibited by the internal electric field, the Fermi level of the system is unique and becomes aligned at both sides of the p–n junction (Figure 1.1b). If we apply an external forward bias with the positive voltage, V_a,

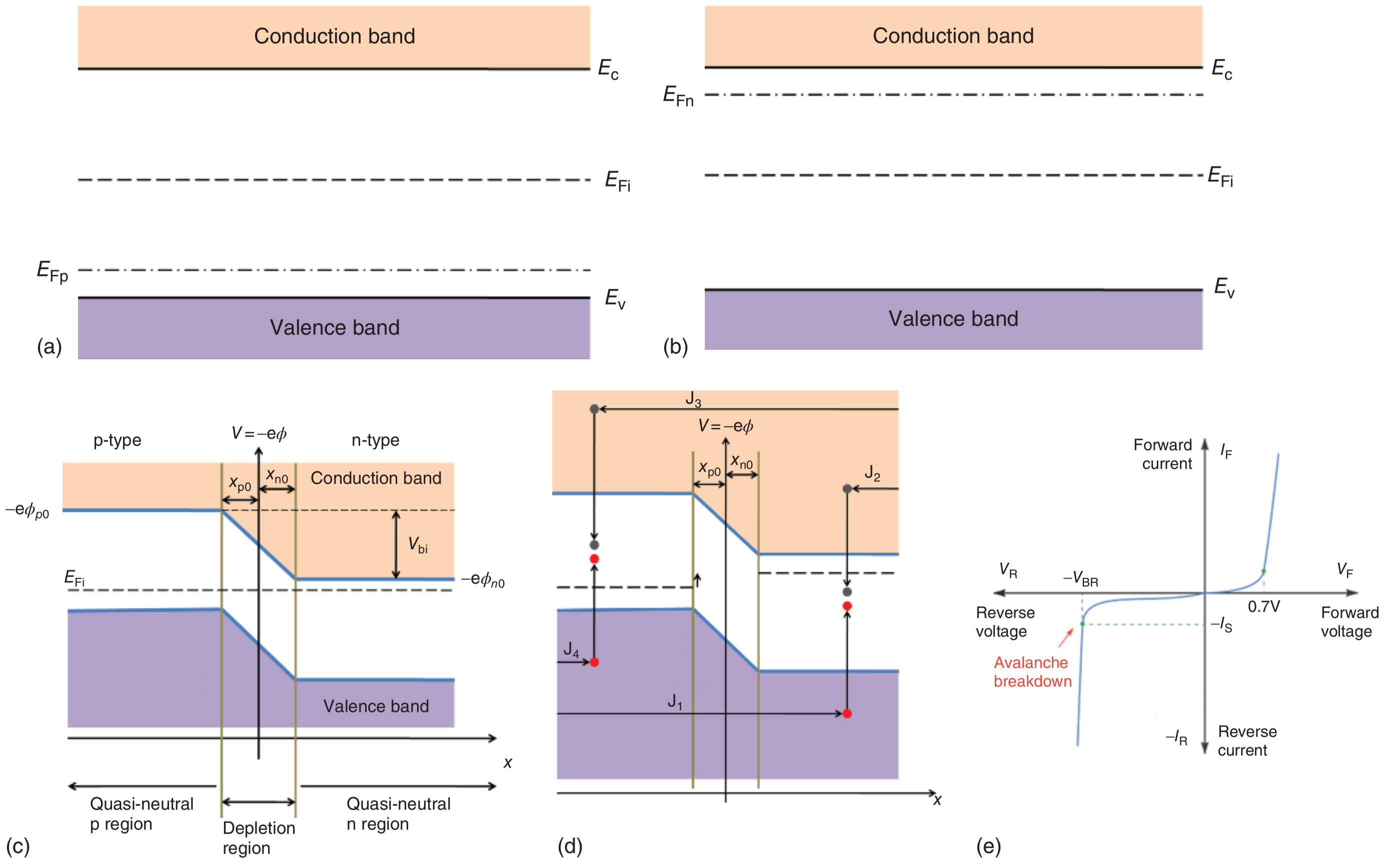

Figure 1.1 The conduction and valence band edges of the p-type and n-type regions of a semiconductor (a) before contact and (b) at the equilibrium when p–n junction is formed. (c and d) The illustration of current generation under forward bias of a p–n junction and (e) the current density–voltage characteristic of a rectifying diode.

applied to the p-region, as illustrated in Figure 1.1c, the field in the depletion region decreases by V_a, so that it will not balance anymore the diffusion of the majority of holes and electrons flowing toward the opposite directions of the p–n junction with the drift current of the minority carriers. This will result in an increased majority hole and electron flow toward opposite directions that both contribute to a net current density (J_{tot}) flowing from the p-type to the n-type regions of the junction. On the contrary, if we apply a negative voltage, V_a, (reverse bias) to the p-type region, the electric field in the depletion region will be strengthened and the associated drift current of the minority carriers will be larger than the diffusion current. As a result, the diode is flowed by a small (because the concentration of minority carriers is extremely low) reverse current (also called as reverse saturation current, J_s). Figure 1.1d illustrates the qualitative behavior of the diode current density, J_{total}, as a function of applied bias, V_a, and shows that diodes based on p–n junctions rectify the current flow as follows:

$$J_{total} = J_S \left[e^{eV_a/(k_B T)} - 1\right] \tag{1.2}$$

where e is the elemental charge, k_B is the Boltzmann constant, and T is the absolute temperature. Equation (1.2) is known as “Shockley” (or diode) equation.

In a Si photovoltaic cell, when a photon is absorbed from the semiconductor material, it creates a free electron in the CB, hence leaving a free hole in the VB (Figure 1.2a). Due to the presence of the “internal” electric field of the p–n junction, the photogenerated holes in the crystal are forced to drift toward the direction of the electric field and accumulate on the p-type region, whereas the photogenerated electrons drift to the opposite direction and accumulate on the n-type region, thereby producing a potential difference termed as open-circuit voltage (V_{OC}) of the photovoltaic cell. Under reverse bias, the accumulated photogenerated holes and electrons flow toward the respective electrodes (the hole selective and electron selective contact, respectively), and thus a significant reverse current (termed as photocurrent, J_{photo}) (Figure 1.2b) flows through the device. A representative current density–voltage (J–V) characteristic of a solar cell operating in the dark and under illumination is shown in Figure 1.2c. In the operation in the dark, we obtain the rectifying behavior of a diode based on the p–n junction. The curve lying beneath the dark curve shows what happens under illumination where a reverse saturation current is obtained even in the absence of an external voltage. This current is called short-circuit current (J_{SC}). If we apply a forward bias, it will compensate the internal electric field, and we will reach a point where it becomes zero and thus there is no current flow within the device. At this point, we obtain the V_{OC} because it is as if the electric circuit is open.

For efficient solar cell operation, both J_{SC} and V_{OC} should be maximized. Moreover, the so-called fill factor (FF) should approach unity. It is the product of the current and voltage, according to the following equation:

$$\mathrm{FF} = \frac{J_{MAX} V_{MAX}}{J_{SC} V_{OC}}, \tag{1.3}$$

where J_{MAX} V_{MAX} gives the maximum power.

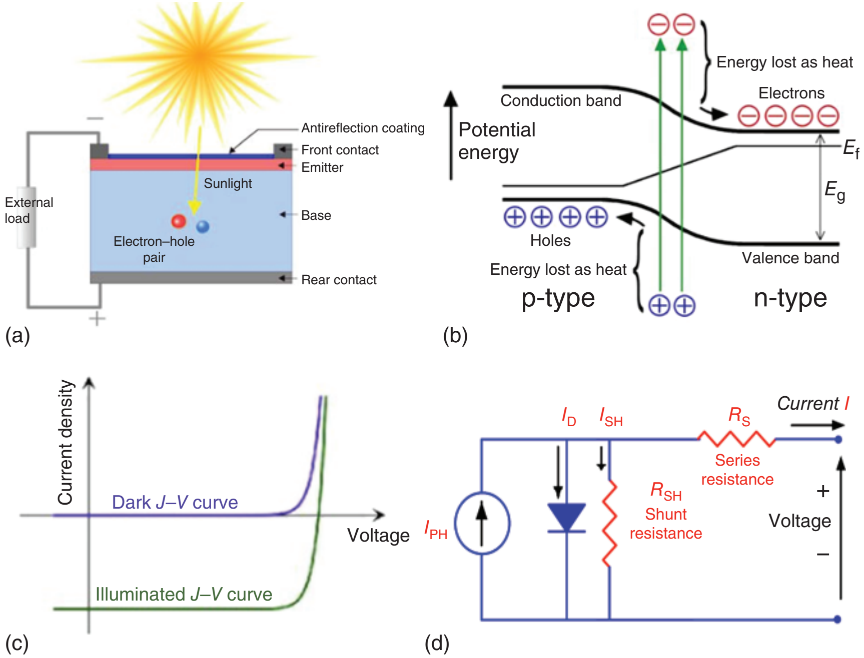

Figure 1.2 (a) The PV cell and (b) the production of electrical current due to the photovoltaic phenomenon taking place in a p–n junction. (c) The *J*–*V* characteristics of a solar cell in dark and under illumination and (d) the equivalent electrical circuit of a solar cell.

Finally, the obtained power conversion efficiency (n or PCE) is calculated according to the following equation:

$$n = \frac{P_{\text{MAX}}}{P_{\text{solar}}} = \text{FF}\frac{J_{\text{SC}}V_{\text{OC}}}{P_{\text{solar}}} \tag{1.4}$$

A photovoltaic cell can be represented by an equivalent electrical circuit presented in Figure 1.2d. By applying Kirchhoff's law, we obtain the device current:

$$I = I_{\text{L}} - I_0\left[\exp\left(\frac{V + IR_{\text{s}}}{nV_{\text{T}}}\right) - 1\right] - \frac{V + IR_{\text{s}}}{R_{\text{sh}}} \tag{1.5}$$

where I_{L} is the photocurrent, I_0 is the reverse saturation current of the diode, R_{s} is the series, R_{sh} is the shunt resistance, and n is the so-called ideality factor. For optimum operation, R_{s} should be minimized, whereas R_{sh} should be maximized.

Using the sun as the photon source (the energy of solar photons ranges from 0.3 to over 4.0 eV), a high-efficiency solar cell can be produced only if we overcome the compromise between photocurrent and photovoltage: a high photocurrent device harvests the majority of the sunlight, whereas a high photovoltage solar cell only harvests the high-energy (UV) photons. There is, hence, a limit in the maximum theoretically achieved efficiency in a single junction device, which is called the Shockley and Queisser limit and is equal to 30% [8]. This can be only achieved by an ideal solar cell harvesting UV to near-infrared (IR) photons up to 1.1 eV.

Silicon solar cells have progressed considerably over the five decades of their existence, and the to-date efficiency record of 26.7% for single-crystal-based Si photovoltaics [9] is approaching the theoretical limit.

1.2.2 Dye-sensitized Solar Cells

Dye-sensitized solar cells (DSSCs) are much different in their architecture and working principle compared to the p–n junction Si photovoltaics. They were first demonstrated in 1972, after the discovery that organic dyes (i.e. chromophores) coated on the zinc oxide (ZnO) electrode of an electrochemical cell could produce electricity upon illumination [10]. Regarding the working mechanism, it was based on the observation that the absorbed photons with energy above the bandgap of the chromophore formed electron–hole (i.e. exciton) pairs in the excited molecule followed by exciton dissociation and electron injection into the wide bandgap metal oxide semiconductor, hence producing electricity (Figure 1.3a). The first demonstration was followed by intense study on ZnO-single crystal electrodes aiming to increase efficiency of these premature DSSCs. However, due to the limited absorption within the visible range of commonly used chromophores and small surface area of ZnO electrode, the PCE remained as low as 1% [12]. Higher efficiencies were obtained upon increasing the porosity of ZnO electrode to enhance the absorption of dye over electrode and, subsequently, the light-harvesting efficiency (LHE) of the system. However, large improvements were obtained in 1991 at Ecole Polytechnique Fédèrale de Lausanne (EPFL), when Michael Grätzel replaced the ZnO electrode with a titanium dioxide (TiO_2) nanoporous layer with a roughness factor of c. 1000; this skyrocketed the DSSCs efficiency up to 7% [13]. These cells, also known as Grätzel cells, were originally co-invented in 1988 by Brian O'Regan and Michael Grätzel at UC Berkeley but were highly optimized by Grätzel's team during the next years [14].

The main constituent of the DSSC cell is a thick (of the order of a few micrometers, μm) mesoporous network of TiO_2, which consists of nanoparticles around 10–30 nm in diameter, prepared as paste in ethanol or water solutions. The paste can be deposited via spin coating, screen printing, or doctor blade onto a glass substrate coated with fluorinated tin oxide (FTO) that serves as the anode electrode (electron selective contact or anode); afterward, the TiO_2 layer is sintered at 400 °C to avoid decomposition. In this "mesoporous" layer, the particles form a network with a high porosity of 40–60%. The mesoporous TiO_2 is sensitized with the organic dye (D) and infiltrated with a redox-active electrolyte [15, 16]. During the next years, this electrolyte was replaced by a solid-state hole transport material (HTM) to avoid device failure due to electrolyte leakage. The photogenerated electrons (produced when dye is photoexcited with sunlight) are transferred from the excited states of the dye into the TiO_2 and then to the front contact (FTO). The oxidized dye (D^+) is subsequently regenerated by the redox active electrolyte through a multi-charge-transfer process; generally, four iodide molecules as well as two holes take place in the regeneration of dye by creating one triiodide and one iodide species (i.e. I_3^-/I^- redox couple, Figure 1.3b) [11, 17]. The triiodide then transfers holes

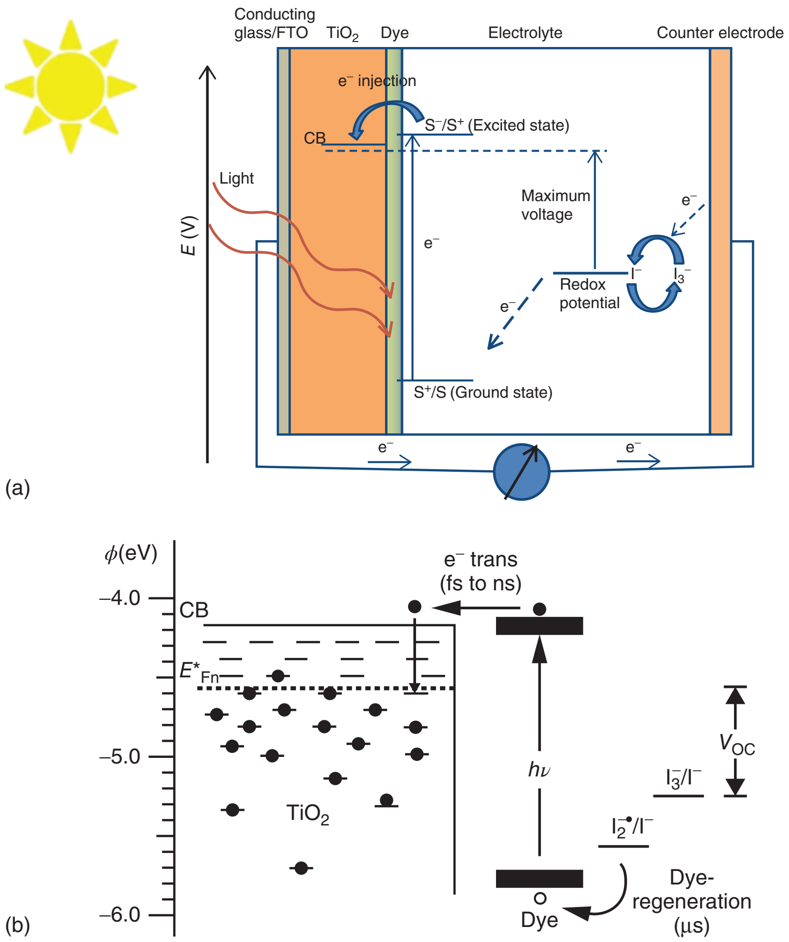

Figure 1.3 (a) The DSSC device architecture and the working mechanism of dye-sensitized solar cell. (b) Illustration of the energy levels at the photoactive heterojunction in a dye-sensitized solar cell. Light is absorbed in the dye at energies higher than the optical bandgap. The open-circuit voltage (V_{OC}) is set by the difference in the quasi-Fermi level for electrons $E_{Fn}{}^{*}$ in the TiO_2 and the equilibrium redox potential of the electrolyte, $I_3{}^{-}/I^{-}$. The loss-in-potential from going from the optical bandgap ($h\nu$) to the open-circuit voltage is clearly illustrated. Source: Reproduced with permission from Snaith et al. [11]/John Wiley & Sons.

to the counter electrode (platinum, Pt), where it is reduced to three iodide species. Hence, the circuit is complete and current flows through the device. In the case of solid-state hole transport-based DSSCs, the regeneration of dye occurs via initial hole transfer to the highest occupied molecular orbital (HOMO) or VB of the hole transporter and then to the cathode electrode to complete the circuit [18].

Grätzel's cell was based on a 10-μm-thick, optically transparent, and colorless with high surface area TiO_2 nanoparticle consisting of film. Deposition of a monolayer of a trimeric ruthenium complex, $RuL_2(\mu\text{-}(CN)Ru(CN)L_2')_2$, where L is

2,2′bipyridine-4,4′-dicarboxylic acid and L′ is 2,2′bipyridine resulted in a significant coloration of TiO_2 film due to the strong absorption of the ruthenium complex within the visible (absorption onset at 750 nm and extinction coefficient at 478 nm of 1.88×10^7 cm^2 mol^{-1}). As a result, the device harvested a high portion of nearly 46% of the incident solar light energy flux and yielded PCE values between 7.1% and 7.9% in simulated solar light (due to a large J_{SC} above 12 mA cm^{-2}) as well as 12% in diffuse daylight. It also exhibited an exceptional stability by sustaining at least five million turnovers without decomposition. In 1993, Nazeeruddin et al. achieved a record efficiency of 10% by using m-X2Bis (2,2,-bipyridyl-4, 4/-dicarboxylate) ruthenium (II) complexes as dye sensitizers with absorption onsets up to 800 nm [19]. Further improvements were reported by the EPFL team in 2011 when they demonstrated 12.3% efficient DSSCs that incorporated a cobalt $Co^{(II/III)}$ tris(bipyridyl)–based redox electrolyte in conjunction with a custom synthesized donor–π-bridge–acceptor zinc porphyrin dye as sensitizer [20]. These authors later demonstrated the record efficiency of 13% holding DSSC, featuring a prototypical structure of a donor–π-bridge–acceptor porphyrin sensitizer that maximized electrolyte compatibility and improved light-harvesting properties [21].

1.2.3 Organic Solar Cells

Organic solar cells (OSCs) are layered structures consisting of an organic photoactive layer sandwiched between two opposite electrodes (Figure 1.4a) [22]. The photoactive layer is based on a blend of a polymer donor with either a fullerene or a non-fullerene acceptor (NFA), hence forming the so-called bulk heterojunction (BHJ) architecture. This is because of the large Coulombic attraction between electron and hole pairs, the so-called Frenkel excitons, due to the low dielectric constants (about 3.5) of common organic semiconductors [23].

For these excitons to dissociate into free carriers, the presence of a two-component system containing the electron donor (D) and the electron acceptor (A) that is similar to that of a p–n junction is necessary [24, 25]. The electron donor should possess a large ionization energy (I_E), whereas the electron acceptor should have a high electron affinity (E_A) for the following reason: Upon photon absorption, an electron is

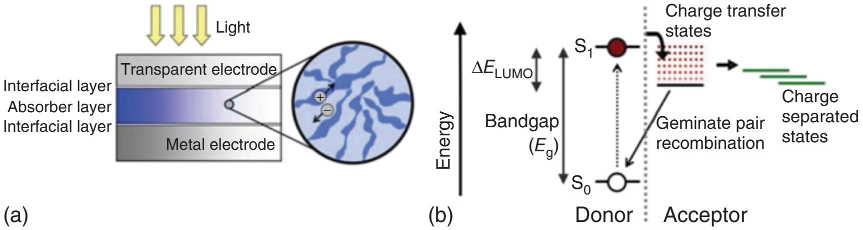

Figure 1.4 (a) Schematic representation of the bulk heterojunction OSC. (b) Organic solar cell energy-level diagram depicting the HOMO and LUMO levels of donor and the formation of charge-transfer states between the donor and acceptor. The process of geminate recombinations is also illustrated. Source: Reproduced with permission from Servaites et al. [22]/Royal Society of Chemistry.

excited from the HOMO to the lowest unoccupied molecular orbital (LUMO) of the donor, hence forming a Frenkel exciton (Figure 1.4b). This exciton then diffuses toward the D:A heterointerface where it dissociates via an energy gradient into a hole and an electron; the latter transfers to the LUMO of the acceptor material and forms a charge transfer (CT) complex, which will be favorable to occur when:

$$E_{\mathrm{A}}^{\mathrm{A}} - E_{\mathrm{A}}^{\mathrm{D}} > U_{\mathrm{D}} \tag{1.6}$$

where $E_{\mathrm{A}}^{\mathrm{A}}$ and $E_{\mathrm{A}}^{\mathrm{D}}$ is the electron affinity of the acceptor and the donor, respectively, and U_{D} is the binding energy of the exciton (of the order of few hundreds of meV). This sets a theoretical maximum for the attainable voltage output in these cells as being the difference between the donor HOMO and acceptor LUMO, given by the following formula:

$$V_{\mathrm{bi}} = E_{\mathrm{LUMO\ (acceptor)}} - E_{\mathrm{HOMO\ (donor)}} \tag{1.7}$$

representing important material design considerations. The electron/hole pair forming the CT state can also be referred to as geminate pair and is highly dependent on the Coulombic attraction between opposite carriers and on the distance that separates these species [26]. If the latter becomes larger than the coulomb capture radius, the geminate pair dissociates into free carriers; otherwise, the geminate pair will recombine across the donor:acceptor interface, the so-called geminate recombination, which constitutes a common loss mechanism in OSCs [27, 28]. The dissociated electrons and holes can then be transported through the acceptor and donor domains, respectively, to the respective electrodes, with electrons being collected at the cathode and holes at the anode.

In the most efficient OSC architecture, the BHJ one, an interpenetrating network of pure donor and acceptor domains, forms the active layer because it strikes a balance between promoting exciton dissociation at D:A interfaces and transports charges through the bulk. This implies that the final and leading loss mechanism in OSCs is charge recombination during charge transport to the electrodes. Key objectives in OSCs are the minimization of energy and charge losses both upon exciton dissociation and through transport within the BHJ device (the latter is crucial due to the low carrier mobility and low diffusion length of the order of 10 nm in organic semiconductors) [1] in order to enhance the efficiency of devices.

A challenging step that contributes to efficient OSCs operation is the charge transport and collection at the electrodes. As most photoactive materials exhibit large energetic differences of their molecular levels, i.e. the HOMO of the donor and the LUMO of the acceptor with the corresponding electrodes, a typical OSC device configuration, fabricated on a transparent rigid (e.g. glass) or flexible substrate, usually comprises a hole transport/extraction layer (HTL/HEL) and an electron transport/extraction layer (ETL/EEL), which are all sandwiched between a high work-function (W_{F}) (anode, the hole-selective contact) and a low W_{F} (cathode, the electron-selective contact) electrode aiming at reducing these differences. In principle, the cathode electrode should have a sufficiently low W_{F} (lower than the LUMO of the acceptor in the active layer), whereas the anode electrode should have a sufficiently high W_{F} (higher than the HOMO of the active layer). An energetic mismatch at any device interface may lead to barriers for charge extraction, to high contact resistance, and to space charge formation and undesirable recombination, thus severely reducing device performance. Other issues that may influence charge transport/extraction, even when interfacial energetic alignment is excellent, are the surface energy mismatch between the various layers and poor interfacial compatibility/morphology.

Examples of electron donor materials used in the photoactive layer of BHJ OSCs are the poly(3-hexylthiophene-2,5-diyl) (P3HT), poly[[9-(1-octylnonyl)-9*H*-carbazole-2,7-diyl]-2,5-thiophenediyl-2,1,3-benzothiadiazole-4,7-diyl-2,5-thiophenediyl] (PCDTBT), and poly((4,8-bis[(2-ethylhexyl)oxy] benzo[1,2-*b*,4,5-*b*′]dithiophene-2,6-diyl)(3-fluoro-2-[(2-ethylhexyl)carbonyl] thieno [3,4-*b*] thiophenediyl)) (PTB7). Materials for electron acceptors are either fullerene such as [6,6]-phenyl C_{71} butyric acid methyl ester ($PC_{71}BM$) and 1′,1″,4′,4″-tetrahydro-di[1,4]methanonaphthaleno-[5,6]fullerene-C_{60}($IC_{60}BA$) or NFAs such as 3,9-bis(2-methylene-((3-(1,1-dicyanomethylene)-6,7-difluoro)-indanone))-5,5,11,11-tetrakis(4-hexylphenyl)-dithieno[2,3-*d*,2′,3′-*d*′]-s-indaceno[1,2-*b*,5,6-*b*′]dithiophene (ITIC-2F). Although the first OSCs reported in 1984 by Tang exhibit very low efficiency of 1% (they were two-layer structures based on a phthalocyanine/perylene carboxylic derivative bilayer absorber) [29], recent developments on NFAs have led to a rapid increase in PCEs, with values of ~17.1% in ternary blend single-junction cells [30] and ~17.3% in double-junction tandem OSCs [31].

1.2.4 Perovskite Solar Cells

Organometallic halide perovskites are materials with a general formula ABX_3 (Figure 1.5a) [34]. Typical examples of A-site substitution are monovalent cations such as organic methylammonium (CH_3NH_3, MA) and formamidinium ($CH(NH_2)_2$, FA) or an inorganic cation such as cesium (Cs) and rubidium (Rb), for B-site occupation, a heavy divalent metal such as lead (Pb) or tin (Sn) and X is a halogen anion (i.e. Cl, Br, and I). The first reported perovskite solar cells (PSCs) had adopted the mesoporous configuration of their DSSC counterparts, and they were hence termed mesoscopic PSCs (MPSCs). They were considered as solid-state DSSCs in which the dye sensitizer has been replaced by an organic–inorganic lead halide perovskite. These first demonstrations of PSCs were based on the 3-dimensional (3D) methylammonium lead iodide ($MAPbI_3$) perovskite, and yielded in mid-2012 PCEs between 6% and 10% [35–37], which were doubled within a few subsequent years only. Immense research to improve device performance by combining novel perovskite materials and their processing techniques led to a remarkable certified PCE of 27.7% in a tandem configuration [38].

In a typical mesoscopic device architecture (Figure 1.5b), a thin (~50 nm) compact TiO_2 layer is first coated on the FTO on glass substrate [32]. Subsequently, the mesoporous TiO_2 layer is deposited on top of the compact layer to serve as the electron transport material (ETM) as well as the scaffold for the infiltration of the perovskite absorber. After its post-annealing at 450 °C, the deposition of the perovskite absorber layer (300–500 nm thick) takes place. The device is completed by the

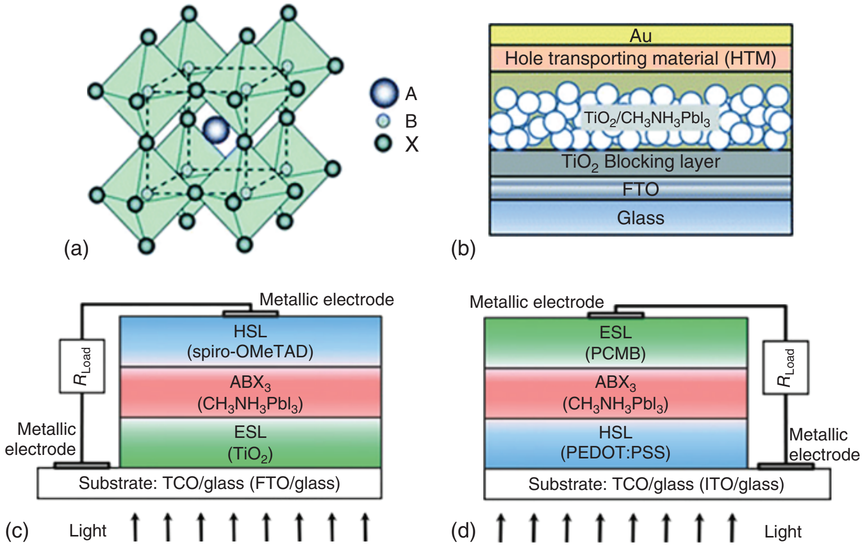

Figure 1.5 (a) Crystal structure of cubic perovskite with general chemical formula ABX_3. Typical device architecture of perovskite solar cells. (b) Device architecture of mesoscopic PSCs. (c) The regular planar (n-i-p) PSC configuration where electrons are collected at the conducting substrate and (d) the inverted planar (p-i-n) architecture where holes are collected at the FTO substrate. Source: (a) and (b) Reproduced with permission from Krishna et al. [32]/Royal Society of Chemistry. (c) and (d) Reproduced with permission from Lopez-Varo et al. [33]/John Wiley & Sons.

deposition of a thin HTM capped with a metal electrode, such as gold (Au) or silver (Ag). The working principle of these devices is quite similar to those of DSSC counterparts and can be split into three steps, i.e. light absorption by perovskite absorber, charge dissociation and separation, and charge transport to respective electrodes. In the first step, light is absorbed by a thin perovskite layer. An optimum bandgap of perovskite (~1.55–1.6 eV) and a high absorption coefficient ($\sim 10^5\ \text{cm}^{-1}$) ensure that maximum visible light is absorbed by the perovskite layer [39]. High-efficiency PSCs require negligible light absorption by the TCO and charge transport/extraction layers such that most absorbed light reaches the perovskite absorber layer. Next is charge dissociation and separation. Herein, the low exciton binding energy of $MAPbI_3$, in the range of a few eV only [40], suggests that photon absorption leads to the generation of free charge carriers. This is extremely desired for a high-efficiency solar cell operation as no external force is required to separate the photogenerated electron–hole pair. The low binding energy and generation of free charge carriers are among the key reasons for high-efficiency PSCs [41]. In other excitonic solar cells, where photogenerated charge pairs (excitons) are bound with higher binding energy (300–500 meV), losses during exciton dissociation and migration account for significant losses [42].

The third step that completes the photovoltaic operation in PSCs is charge extraction toward respective electrodes. This requires the injection of at least one type of charge carriers from the perovskite absorber layer into the transport material (and blocking of the other type). Charge selective layers that allow only one type of charge carriers to be extracted are hence employed alongside the perovskite layer to facilitate their extraction. These selective contacts heavily influence interfacial recombination, charge accumulation and extraction, and consequently play a critical role in determining photovoltaic parameters in PSCs.

Other architectures besides the mesoscopic cells are the regular planar (n-i-p) or inverted planar (p-i-n) structures (Figure 1.5c,d) in which the mesoporous TiO_2 layer is omitted and the perovskite planar absorber is deposited directly either on the electron transport (n-i-p) or the hole transport (p-i-n) material, which guides photogenerated charges toward their respective electrode [33, 43]. These planar devices can be processed at temperature below 150 °C and, therefore, are advantageous for mass production.

An interesting aspect while designing a PSC is its tunable electrical properties. From a typically intrinsic perovskite, their electrical conductivity can be tuned to n- or p-type by manipulating its defects density. Typical 3D halide perovskite, for example, $MAPbI_3$ or $FAPbI_3$, shows an optimum direct bandgap (E_g) of ~1.6 and 1.5 eV, respectively [2–4]. Theoretical calculations predict that an optimized single junction $MAPbI_3$ PSC can deliver PCE of ~31%. This efficiency corresponds to a photocurrent density (J_{SC}) of 26 mA cm^{-2}, an open-circuit voltage (V_{OC}) of 1.3 V, and FF of 91% [44]. However, this requires that there be no non-radiative losses within the bulk of the perovskite as well as the device interfaces. The PSCs still have to overcome losses due to bulk and interfacial defects to reach their Shockley Queisser limit.

Another important device architecture with triple-mesoscopic layer, which replaces expensive metal contacts such as Au or Ag with carbon (C), is printable MPSCs, also called as Han Cells or Wuhan Cells [45–47]. Such structures, even though lagging in performance compared to their mesoporous or planar counterparts, provide improved operational stability and also are cost-effective . Moreover, carbon composite electrodes can offer an affordable, conductive alternative with abundant sources and blends of carbon black (CB) and graphite (G) being also chemically resistant toward oxidation/reactions and can be printed in batch or continuous roll-to-roll processing, hence offering the possibility for fully printable large area devices [48, 49].

1.3 The Typical Structures of PSC

1.3.1 Mesoscopic Structure

MPSCs are based on a mesoporous ETL such as TiO_2 and SnO_2 or an insulating scaffold like Al_2O_3 and ZrO_2 [50]. The perovskite absorber is then infiltrated in the mesoporous metal oxide scaffold layer, followed by a solid-state hole conductor, which is deposited on top of the perovskite layer (Figure 1.6a). The reader is referred to Section 1.2.4 for more details about the MPSC architecture. Notably, the most efficient PSCs are the mesoscopic ones as they allow larger portion of the incident light

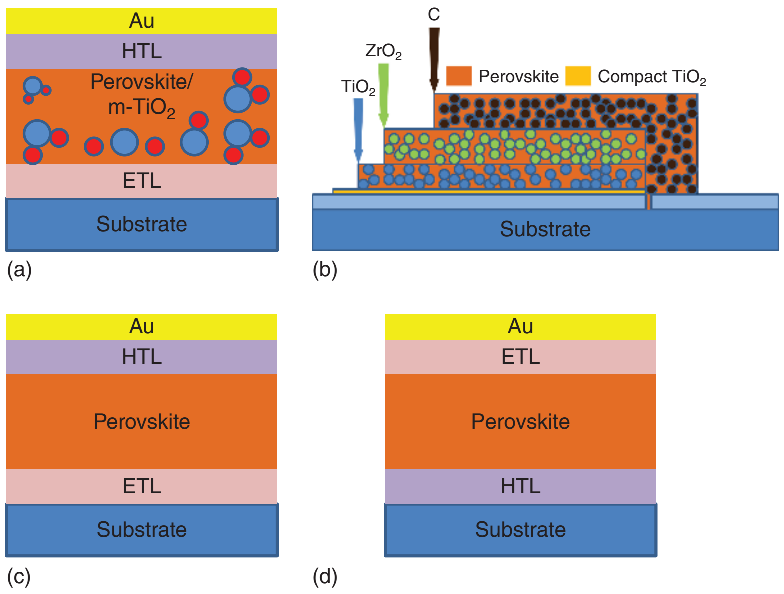

Figure 1.6 Device architecture for (a) mesoscopic (b) triple layer, (c) regular planar n-i-p, and (d) inverted planar p-i-n structure.

to be absorbed while also exhibiting a high surface area between the perovskite absorber and the bottom ETL. Even though in early years high-temperature sintering of the metal oxide layer was generally applied, it was later revealed that using metal oxides alternative to TiO_2 such as SnO_2 that demand post-treatment at lower temperatures can lead to the possibility of MPSCs fabrication upon flexible substrates and multifunctional device architectures [51].

1.3.2 Triple-mesoscopic Layer Structure

Besides the mesoscopic structure using a single mesoporous metal oxide at the bottom electrode, solar cells with a double layer consisting of mesoporous oxides such as TiO_2 and ZrO_2, where the perovskite film is infiltrated, have been successfully demonstrated (Figure 1.6b) [46]. In the first demonstration of this device structure, which was printable, the metal halide perovskite was infiltrated into the mesoporous TiO_2/ZrO_2 scaffold by drop-casting a solution through the printed porous carbon (C) layer, which served as the top cathode electrode [46]. The perovskite precursor solution contained PbI_2 in g-butyrolactone mixed with MA and 5-aminovaleric acid (5-AVA) cations that formed a mixed-cation $(5\text{-AVA})_x(MA)_{1-x}PbI_3$ perovskite. The hole-conductor–free cell with the simple mesoscopic $TiO_2/ZrO_2/C$ triple layer as a scaffold to host the perovskite absorber yielded a PCE of 12.84% and good long-term stability.

However, for these printable cells, it is difficult to control the crystallization mechanism of perovskite owing to the complicated triple-layer mesoporous structure. Recently, a solvent evaporation-controlled crystallization method has been reported that enabled ideal crystallization of the perovskite absorber in the mesoscopic structure [52]. It was based on the adjustment of the evaporation rate of solvent during annealing in the mesoporous structures. The FP–MPSCs exhibited a homogeneous pore filling in the triple-layer structure without any additives and achieved a stabilized PCE of 16.26% using ternary-cation perovskite absorber.

1.3.3 Regular Planar n-i-p Structure

This structure is quite similar to thin-film inorganic and OSCs. It consists of a bottom transparent electron selective electrode (anode), an n-type thin compact ETL, the perovskite absorber layer, the p-type HTL, and the top high W_F metal cathode (hole selective electrode) (Figure 1.6c). This configuration is based on the mesoscopic structure, but it does not include the mesoporous metal oxide layer. One of the maximum efficiencies achieved in this architecture (PCE of 21.6%) was based on an EDTA-modified SnO_2 instead of TiO_2 as the ETL and Cs-doped $FAPbI_3$ as the perovskite absorber, along with a Spiro-OMeTAD as the HTL [53]. Notably, PSCs with the n-i-p structure undergo severe degradation when using organic HTLs while those with inorganic HTMs not only achieve good PCE but also show comparatively better device stability.

1.3.4 Inverted Planar p-i-n Structure

This device architecture was borrowed from the OSCs technology where it is considered as the regular structure. It has a reverse sequence of ETLs and HTLs compared to the n-i-p structure (Figure 1.6d). The bottom HTL is commonly an organic p-type semiconductor, whereas the top ETL is based on fullerene derivatives [54]. However, appropriate p-type metal oxides such as NiO have been also applied as HTMs with sufficient success in terms of efficiency but, most importantly, stability to ambient air-induced degradation [54].

References

1 Saidel, M.A., Reis, T.M., and Prado, F.A.A. (2009). Carbon credits and energy efficiency. *International Journal of Green Energy* 6 (3): 312–322.

2 Luque, A. and Hegedus, S. (2011). *Handbook of Photovoltaic Science and Engineering*. Wiley.

3 Adams, W.G. and Day, R.E. (1877). V. The action of light on selenium. *Proceedings of the Royal Society of London* 25 (171–178): 113–117.

4 Chen, T., Qiu, L., Yang, Z., and Peng, H. (2013). Novel solar cells in a wire format. *Chemical Society Reviews* 42 (12): 5031–5041.

5 Fritts, C.E. (1883). ART. LII.--On a new form of selenium cell, and some electrical discoveries made by its use. *American Journal of Science (1880–1910)* 26 (156): 465.

6 Chapin, D.M., Fuller, C.S., and Pearson, G.L. (1954). A new silicon p-n junction photocell for converting solar radiation into electrical power. *Journal of Applied Physics* 25 (5): 676–677.

7 Chapin, D. M., Fuller, C. S.,and Pearson, G. L. (1957), inventors Google Patents US2780765A, assignee. Solar energy converting apparatus.

8 Shockley, W. and Queisser, H.J. (1961). Detailed balance limit of efficiency of p-n junction solar cells. *Journal of Applied Physics* 32 (3): 510–519.

9 Green, M.A., Hishikawa, Y., Dunlop, E.D. et al. (2018). Solar cell efficiency tables. *Progress in Photovoltaics: Research and Applications* 26: 427.

10 Tributsch, H. and Calvin, M. (1971). Electrochemistry of excited molecules: photo-electrochemical reactions of chlorophylls. *Photochemistry and Photobiology* 14 (2): 95–112.

11 Snaith, H.J. (2010). Estimating the maximum attainable efficiency in dye-sensitized solar cells. *Advanced Functional Materials* 20 (1): 13–19.

12 Tsubomura, H., Matsumura, M., Nomura, Y., and Amamiya, T. (1976). Dye sensitised zinc oxide: aqueous electrolyte: platinum photocell. *Nature* 261 (5559): 402–403.

13 O'Regan, B. and Grätzel, M. (1991). A low-cost, high-efficiency solar cell based on dye-sensitized colloidal TiO_2 films. *Nature* 353 (6346): 737–740.

14 Nazeeruddin, M.K., Baranoff, E., and Grätzel, M. (2011). Dye-sensitized solar cells: a brief overview. *Solar Energy* 85 (6): 1172–1178.

15 Altobello, S., Bignozzi, C., Caramori, S. et al. (2004). Sensitization of TiO_2 with ruthenium complexes containing boronic acid functions. *Journal of Photochemistry and Photobiology A: Chemistry* 166 (1–3): 91–98.

16 Kunzmann, A., Valero, S., Sepúlveda, Á.E. et al. (2018). Hybrid dye-titania nanoparticles for superior low-temperature dye-sensitized solar cells. *Advanced Energy Materials* 8 (12): 1702583.

17 Peter, L.M. (2007). Dye-sensitized nanocrystalline solar cells. *Physical Chemistry Chemical Physics* 9 (21): 2630–2642.

18 Montanari, I., Nelson, J., and Durrant, J.R. (2002). Iodide electron transfer kinetics in dye-sensitized nanocrystalline TiO_2 films. *Journal of Physical Chemistry B* 106 (47): 12203–12210.

19 Nazeeruddin, M.K., Kay, A., Rodicio, I. et al. (1993). Conversion of light to electricity by cis-X2bis(2,2'-bipyridyl-4,4'-dicarboxylate)ruthenium(II) charge-transfer sensitizers (X = Cl-, Br-, I-, CN-, and SCN-) on nanocrystalline titanium dioxide electrodes. *Journal of the American Chemical Society* 115: 6382.

20 Yella, A., Lee, H.-W., Tsao, H.N. et al. (2011). Porphyrin-sensitized solar cells with cobalt (II/III)–based redox electrolyte exceed 12 percent efficiency. *Science* 334 (6056): 629–634.

21 Mathew, S., Yella, A., Gao, P. et al. (2014). Dye-sensitized solar cells with 13% efficiency achieved through the molecular engineering of porphyrin sensitizers. *Nature Chemistry* 6 (3): 242–247.

22 Servaites, J.D., Ratner, M.A., and Marks, T.J. (2011). Organic solar cells: a new look at traditional models. *Energy & Environmental Science* 4 (11): 4410–4422.

23 Ameri, T., Khoram, P., Min, J., and Brabec, C.J. (2013). Organic ternary solar cells: a review. *Advanced Materials* 25 (31): 4245–4266.

24 Kniepert, J., Schubert, M., Blakesley, J.C., and Neher, D. (2011). Photogeneration and recombination in P_3HT/PCBM solar cells probed by time-delayed collection field experiments. *Journal of Physical Chemistry Letters* 2 (7): 700–705.

25 Ran, N.A., Roland, S., Love, J.A. et al. (2017). Impact of interfacial molecular orientation on radiative recombination and charge generation efficiency. *Nature Communications* 8 (1): 1–9.

26 Elumalai, N.K. and Uddin, A. (2016). Open circuit voltage of organic solar cells: an in-depth review. *Energy & Environmental Science* 9 (2): 391–410.

27 Weickert, J., Dunbar, R.B., Hesse, H.C. et al. (2011). Nanostructured organic and hybrid solar cells. *Advanced Materials* 23 (16): 1810–1828.

28 Brabec, C., Scherf, U., and Dyakonov, V. (2011). *Organic Photovoltaics: Materials, Device Physics, and Manufacturing Technologies*. Wiley.

29 Tang, C.W. (1986). Two-layer organic photovoltaic cell. *Applied Physics Letters* 48 (2): 183–185.

30 Lin, Y., Firdaus, Y., Nugraha, M.I. et al. (2020). 17.1% efficient single-junction organic solar cells enabled by n-type doping of the bulk-heterojunction. *Advanced Science* 7 (7): 1903419.

31 Meng, L., Zhang, Y., Wan, X. et al. (2018). Organic and solution-processed tandem solar cells with 17.3% efficiency. *Science* 361 (6407): 1094–1098.

32 Krishna, A. and Grimsdale, A.C. (2017). Hole transporting materials for mesoscopic perovskite solar cells–towards a rational design? *Journal of Materials Chemistry A* 5 (32): 16446–16466.

33 Lopez-Varo, P., Jiménez-Tejada, J.A., García-Rosell, M. et al. (2018). Device physics of hybrid perovskite solar cells: theory and experiment. *Advanced Energy Materials* 8 (14): 1702772.

34 Saparov, B. and Mitzi, D.B. (2016). Organic–inorganic perovskites: structural versatility for functional materials design. *Chemical Reviews* 116 (7): 4558–4596.

35 Alsulami, A., Griffin, J., Alqurashi, R. et al. (2016). Thermally stable solution processed vanadium oxide as a hole extraction layer in organic solar cells. *Materials* 9 (4): 235.

36 Burschka, J., Pellet, N., Moon, S.-J. et al. (2013). Sequential deposition as a route to high-performance perovskite-sensitized solar cells. *Nature* 499 (7458): 316–319.

37 Kim, H.-S., Lee, C.-R., Im, J.-H. et al. (2012). Lead iodide perovskite sensitized all-solid-state submicron thin film mesoscopic solar cell with efficiency exceeding 9%. *Scientific Reports* 2 (1): 1–7.

38 Pham, H., Kho, T.C., Phang, P. et al. (2020). High efficiency perovskite-silicon tandem solar cells: effect of surface coating versus bulk incorporation of 2D perovskite. *Advanced Energy Materials* 10 (32): 2002139.

39 De Wolf, S., Holovsky, J., Moon, S.-J. et al. (2014). Organometallic halide perovskites: sharp optical absorption edge and its relation to photovoltaic performance. *Journal of Physical Chemistry Letters* 5 (6): 1035–1039.

40 Chen, W., Zhou, Y., Chen, G. et al. (2019). Alkali chlorides for the suppression of the interfacial recombination in inverted planar perovskite solar cells. *Advanced Energy Materials* 9 (19): 1803872.

41 Collavini, S., Völker, S.F., and Delgado, J.L. (2015). Understanding the outstanding power conversion efficiency of perovskite-based solar cells. *Angewandte Chemie International Edition* 54 (34): 9757–9759.

42 Bai, Y., Chen, H., Xiao, S. et al. (2016). Effects of a molecular monolayer modification of NiO nanocrystal layer surfaces on perovskite crystallization and interface contact toward faster hole extraction and higher photovoltaic performance. *Advanced Functional Materials* 26 (17): 2950–2958.

43 Im, J.-H., Lee, C.-R., Lee, J.-W. et al. (2011). 6.5% efficient perovskite quantum-dot-sensitized solar cell. *Nanoscale* 3 (10): 4088–4093.

44 Sha, W.E., Ren, X., Chen, L., and Choy, W.C. (2015). The efficiency limit of $CH_3NH_3PbI_3$ perovskite solar cells. *Applied Physics Letters* 106 (22): 221104.

45 Ku, Z.L., Rong, Y.G., Xu, M. et al. (2013). Full printable processed mesoscopic $CH_3NH_3PbI_3/TiO_2$ heterojunction solar cells with carbon counter electrode. *Scientific Reports* 3.

46 Mei, A.Y., Li, X., Liu, L.F. et al. (2014). A hole-conductor-free, fully printable mesoscopic perovskite solar cell with high stability. *Science* 345 (6194): 295–298.

47 Rong, Y.G., Hu, Y., Mei, A.Y. et al. (2018). Challenges for commercializing perovskite solar cells. *Science* 361 (6408).

48 Han, H., Bach, U., Cheng, Y.-B. et al. (2009). A design for monolithic all-solid-state dye-sensitized solar cells with a platinized carbon counterelectrode. *Applied Physics Letters* 94 (10): 103102.

49 He, Q., Yao, K., Wang, X. et al. (2017). Room-temperature and solution-processable Cu-doped nickel oxide nanoparticles for efficient hole-transport layers of flexible large-area perovskite solar cells. *ACS Applied Materials & Interfaces* 9 (48): 41887–41897.

50 Etgar, L., Gao, P., Xue, Z. et al. (2012). Mesoscopic $CH_3NH_3PbI_3/TiO_2$ heterojunction solar cells. *Journal of the American Chemical Society* 134 (42): 17396–17399.

51 Ball, J.M., Lee, M.M., Hey, A., and Snaith, H.J. (2013). Low-temperature processed meso-superstructured to thin-film perovskite solar cells. *Energy & Environmental Science* 6 (6): 1739–1743.

52 Wang, Q., Zhang, W., Zhang, Z. et al. (2020). Crystallization control of ternary-cation perovskite absorber in triple-mesoscopic layer for efficient solar cells. *Advanced Energy Materials* 10 (5): 1903092.

53 Yang, D., Yang, R., Wang, K. et al. (2018). High efficiency planar-type perovskite solar cells with negligible hysteresis using EDTA-complexed SnO_2. *Nature Communications* 9 (1): 1–11.

54 Tang, J., Jiao, D., Zhang, L. et al. (2018). High-performance inverted planar perovskite solar cells based on efficient hole-transporting layers from well-crystalline NiO nanocrystals. *Solar Energy* 161: 100–108.